Three-dimensional quaternionic condensations, Hopf invariants, and skyrmion lattices with synthetic spin-orbit coupling

Yi Li,[1,2] Xiangfa Zhou,[3,4] and Congjun Wu[2]

[1]*Princeton Center for Theoretical Science, Princeton University, Princeton, New Jersey 08544, USA*

[2]*Department of Physics, University of California, San Diego, La Jolla, California 92093, USA*

[3]*Key Laboratory of Quantum Information, Chinese Academy of Sciences, University of Science and Technology of China, Hefei 230026, China*

[4]*Synergetic Innovation Center of Quantum Information and Quantum Physics, University of Science and Technology of China, Hefei 230026, China*

(Received 10 February 2016; published 14 March 2016)

We study the topological configurations of the two-component condensates of bosons with the three-dimensional (3D) $\vec{\sigma}\cdot\vec{p}$ Weyl-type spin-orbit coupling subject to a harmonic trapping potential. The topology of the condensate wave functions manifests in the quaternionic representation. In comparison to the U(1) complex phase, the quaternionic phase manifold is S^3 and the spin orientations form the S^2 Bloch sphere through the first Hopf mapping. The spatial distributions of the quaternionic phases exhibit the 3D skyrmion configurations, and the spin distributions possess nontrivial Hopf invariants. Spin textures evolve from the concentric distributions at the weak spin-orbit coupling regime to the rotation symmetry-breaking patterns at the intermediate spin-orbit coupling regime. In the strong spin-orbit coupling regime, the single-particle spectra exhibit the Landau-level-type quantization. In this regime, the three-dimensional skyrmion lattice structures are formed when interactions are below the energy scale of Landau-level mixings. Sufficiently strong interactions can change condensates into spin-polarized plane-wave states or superpositions of two plane waves exhibiting helical spin spirals.

DOI: 10.1103/PhysRevA.93.033628

I. INTRODUCTION

Quantum-mechanical wave functions generally speaking are complex valued. However, for the single-component boson systems, their ground-state many-body wave functions are highly constrained, which are usually positive definite [1], as a consequence of the Perron-Frobenius theorem in the mathematical context of matrix analysis [2]. This is a generalization of the "no-node" theorem of the single-particle quantum mechanics, for example, both the ground-state wave functions of harmonic oscillators and hydrogen atoms are nodeless. Although the positive definiteness does not apply to the many-body fermion wave functions because Fermi statistics necessarily leads to nodal structures, it remains valid for many-body boson systems. It applies under the following conditions: the Laplacian type kinetic energy, the arbitrary single-particle potential, and the coordinate-dependent interactions. The positive definiteness of the ground-state wave functions implies that time-reversal (TR) symmetry cannot be spontaneously broken in conventional Bose-Einstein condensates (BECs), such as the superfluid ^{4}He and most ground-state BECs of ultracold alkali bosons [3].

It would be interesting to seek unconventional BECs beyond the constraint of positive-definite condensate wave functions [4,5]. The spin-orbit coupled boson systems are an ideal platform to study this class of exotic states of bosons, which can spontaneously break the TR symmetry. In addition to a simple Laplacian, the kinetic energy contains the spin-orbit coupling term linearly dependent on momentum. If the bare interaction is spin independent, the condensate wave functions are heavily degenerate. An "order-from-disorder" calculation based on the zero-point energy of the Bogoliubov spectra was performed to select the condensate configuration [4]. Inside the harmonic trap, it is predicted that the condensates spontaneously develop the half-quantum vortex coexisting with two-dimensional (2D) skyrmion-type spin textures [6]. Experimentally, spin-orbit coupled bosons have been realized in exciton systems in semiconducting quantum wells. Spin texture configurations similar to those predicted in Ref. [6] have been observed [7,8]. On the other hand, the progress of synthetic artificial gauge fields in ultracold atomic gases greatly stimulates the investigation of the above exotic states of bosons [9,10]. Extensive studies have been performed for bosons with the 2D Rashba spin-orbit coupling, which exhibit various spin structures arising from the competitions among the spin-orbit coupling, interaction, and confining trap energy [6,11–18].

Most studies so far have been on the two-dimensional spin-orbit coupled bosons. It would be interesting to further consider the unconventional condensates of bosons with the three-dimensional (3D) Weyl-type spin-orbit coupling, the experimental realization of which has been proposed by the authors through atom-light interactions in a combined tripod and tetrapod level system [19] and also by Anderson *et al.* [20]. As will be shown below, the quaternion representation provides a natural and most beautiful description of the topological condensation configurations. Quaternions are an extension of complex numbers as the first discovered noncommutative division algebra, which has provided a new formulation of quantum mechanics [21–23]. Similarly to complex numbers the phases of which span a unit circle S^1, the quaternionic phases span a three-dimensional unit sphere S^3. The spin distributions associated with quaternionic wave functions are obtained through the first Hopf map $S^3 \to S^2$ as will be explained below. It would be interesting to search for BECs with nontrivial topological defects associated with the quaternionic phase structure. It will be a new class of unconventional BECs beyond the "no-node" theorem breaking TR symmetry spontaneously.

In this paper, we consider the unconventional condensate wave functions with the 3D Weyl-type spin-orbit coupling

$\vec{\sigma}\cdot\vec{p}$. The condensation wave functions exhibit topologically nontrivial configurations as 3D skyrmions, and spin-density distributions are also nontrivial with nonzero Hopf invariants. These topological configurations can be best represented as defects of quaternion phase distributions. Spatial distributions of the quaternionic phase textures and spin textures are concentric at weak spin-orbit couplings. As increasing spin-orbit coupling, these textures evolve to lattice structures which are the 3D quaternionic analogy of the 2D Abrikosov lattice of the usual complex condensate.

The rest of this paper is organized as follows. In Sec. II, we define the model Hamiltonian. In Sec. III, the condensate wave functions in the weak spin-orbit regime are studied. Topological analyses on the skyrmion configurations and Hopf invariants are performed by using the quaternion representation. In Sec. IV, the skyrmion lattice configuration of the spin textures is studied in the intermediate and strong spin-orbit coupling regimes. In Sec. V, superpositions of plane-wave condensate configurations are studied. Conclusions are made in Sec. VI.

II. THE MODEL HAMILTONIAN

We consider a two-component boson system with the 3D spin-orbit coupling of the $\vec{\sigma}\cdot\vec{p}$ type confined in a harmonic trap. The free part of the Hamiltonian is defined as

$$H_0=\int d^3\vec{r}\,\psi_\gamma^\dagger(\vec{r})\Big\{-\frac{\hbar^2\vec{\nabla}^2}{2m}+i\hbar\lambda\vec{\sigma}_{\gamma\delta}\cdot(\vec{\nabla})+\frac{1}{2}m\omega^2\vec{r}^{\,2}\Big\}\psi_\delta(\vec{r}),\tag{1}$$

where γ and δ equal $\uparrow$ and $\downarrow$ referring to two internal states of bosons; $\vec{\sigma}$ are Pauli matrices; m is the boson mass; λ is the spin-orbit coupling strength with the unit of velocity; ω is the trap frequency. At the single-particle level, Eq. (1) satisfies the Kramer-type time-reversal symmetry of $T=(-i\sigma_2)C$ with the property of $T^2=-1$. However, parity is broken by spin-orbit coupling. In the absence of the trap, good quantum numbers for the single-particle states are the eigenvalues ±1 of helicity $\vec{\sigma}\cdot\vec{p}/|p|$, where p is the momentum. This results in two branches of dispersions

$$\epsilon_\pm(\vec{k})=\frac{\hbar^2}{2m}(k\mp k_{\rm SO})^2,\tag{2}$$

where $\hbar k_{\rm SO}=m\lambda$. The lowest single-particle energy states lie in the sphere with the radius $k_{\rm SO}$ denoted as the spin-orbit sphere. It corresponds to a spin-orbit length scale $l_{\rm SO}=1/k_{\rm SO}$ in real space. The harmonic trap has a natural length scale $l_T=\sqrt{\frac{\hbar}{m\omega}}$, and thus the dimensionless parameter $\alpha=l_Tk_{\rm SO}$ describes the relative spin-orbit coupling strength.

As for the interaction Hamiltonian, we use the contact s-wave scattering interaction defined as

$$H_{\rm int}=\frac{g_{\gamma\delta}}{2}\int d^3\vec{r}\,\psi_\gamma^\dagger(\vec{r})\psi_\delta^\dagger(\vec{r})\psi_\delta(\vec{r})\psi_\gamma(\vec{r}).\tag{3}$$

Two different interaction parameters are allowed, including the intra- and intercomponent ones defined as $g_{\uparrow\uparrow}=g_{\downarrow\downarrow}=g$, and $g_{\uparrow\downarrow}=cg$, where c is a constant.

In the previous study of the 2D Rashba spin-orbit coupling with harmonic potentials [6,17], the single-particle eigenstates are intuitively expressed in the momentum representation: the low-energy state lies around a ring in momentum space, and the harmonic potential becomes the planar rotor operator on this ring subject to a π flux, which quantizes the angular momentum j_z to half integers. A similar picture also applies in three dimensions [6,24]. The low-energy states are around the spin-orbit sphere. In the projected low-energy Hilbert space, the eigenvectors read

$$\psi_+(\vec{k})=\left(\cos\frac{\theta_k}{2},\sin\frac{\theta_k}{2}e^{i\phi_k}\right)^T.\tag{4}$$

The harmonic potential is again a rotor Hamiltonian on the spin-orbit sphere subject to the Berry gauge connection as

$$V_{tp}=\tfrac{1}{2}m(i\nabla_k-\vec{A}_k)^2\tag{5}$$

with the moment of inertial $I=M_kk_{\rm SO}^2$ and $M_k=\hbar^2/(m\omega^2)$. $\vec{A}_k=i\langle\psi_+(\vec{k})|\nabla_k|\psi_+(\vec{k})\rangle$ is the vector potential of a U(1) magnetic monopole, which quantizes the angular momentum j to half integers. While the radial energy is still quantized in terms of $\hbar\omega$, the angular energy dispersion with respect to j is strongly suppressed at large values of α as

$$E_{n_r,j,j_z}\approx\left(n_r+\frac{j(j+1)}{2\alpha^2}\right)\hbar\omega+\text{const},\tag{6}$$

where n_r is the radial quantum number. As further shown in Ref. [19], in the case $\alpha\gg1$, all the states with the same n_r but different j and j_z are nearly degenerate, and thus can be viewed as one 3D Landau level with spherical symmetry but broken parity. If filled with fermions, the system belongs to the Z_2 class of 3D strong topological insulators.

Now we load the system with bosons. The interaction energy scale is defined as $E_{\rm int}=gN_0/l_T^3$, where N_0 is the total particle number in the condensate. The corresponding dimensionless parameter is $\beta=E_{\rm int}/\hbar\omega$. At the Hartree-Fock level, the Gross-Pitaevskii energy functional is defined in terms of the condensate wave function $\Psi=(\Psi_\uparrow,\Psi_\downarrow)^T$ as

$$E=\int d^3\vec{r}(\Psi_\uparrow^\dagger,\Psi_\downarrow^\dagger)\Big\{-\frac{\hbar^2\nabla^2}{2m}-i\lambda\hbar\vec{\nabla}\cdot\vec{\sigma}+\frac{1}{2}m\omega^2r^2+g\begin{pmatrix}n_\uparrow+cn_\downarrow & 0\\ 0 & cn_\uparrow+n_\downarrow\end{pmatrix}\Big\}\begin{pmatrix}\Psi_\uparrow\\ \Psi_\downarrow\end{pmatrix},\tag{7}$$

where $n_{\uparrow,\downarrow}(\vec{r})=N_0|\Psi_{\uparrow,\downarrow}(\vec{r})|^2$ are the particle densities of two components, respectively, and $\Psi(\vec{r})$ is normalized as $\int d^3\vec{r}\Psi^\dagger(\vec{r})\Psi(\vec{r})=1$. The condensate wave function $\Psi(\vec{r})$ is solved numerically by using the standard method of imaginary time evolution. The dimensionless form of the Gross-Pitaevskii equation is

$$E'=\int d^3\vec{r}'(\tilde{\Psi}_\uparrow^\dagger,\tilde{\Psi}_\downarrow^\dagger)\Big\{-\frac{\vec{\nabla}'^2}{2}-i\alpha\vec{\nabla}'\cdot\vec{\sigma}+\frac{r'^2}{2}+\beta\begin{pmatrix}\tilde{n}_\uparrow+c\tilde{n}_\downarrow & 0\\ 0 & c\tilde{n}_\uparrow+\tilde{n}_\downarrow\end{pmatrix}\Big\}\begin{pmatrix}\tilde{\Psi}_\uparrow\\ \tilde{\Psi}_\downarrow\end{pmatrix},\tag{8}$$

where $E'=E/(\hbar\omega)$, $\vec{\nabla}'=l_T\vec{\nabla}$; $\vec{r}'=\vec{r}/l_T$; $\tilde{\Psi}_\uparrow$ and $\tilde{\Psi}_\downarrow$ are the renormalized condensate wave functions satisfying $\int d^3r'|\tilde{\Psi}_\uparrow|^2+|\tilde{\Psi}_\downarrow|^2=1$; $\tilde{n}_\uparrow=|\tilde{\Psi}_\uparrow|^2$ and $\tilde{n}_\downarrow=|\tilde{\Psi}_\downarrow|^2$.

III. THE WEAK SPIN-ORBIT COUPLING REGIME

In this section, we consider the condensate configuration in the limit of weak spin-orbit coupling, say, $\alpha \sim 1$. In this regime, the single-particle spectra still resemble those of the harmonic trap. We study the case that interactions are not strong enough to mix states with different angular momenta.

A. The spin-orbit coupled condensate

In this regime, the condensate wave function Ψ remains the same symmetry structure as the single-particle wave function over a wide range of interaction parameter β, i.e., Ψ remains the eigenstates of $j = \frac{1}{2}$ as confirmed numerically below. Ψ can be represented as

$$\Psi_{j=j_z=\frac{1}{2}}(r,\hat{\Omega}) = f(r)Y^{+}_{j,j_z}(\hat{\Omega}) + ig(r)Y^{-}_{j,j_z}(\hat{\Omega}), \tag{9}$$

where $f(r)$ and $g(r)$ are real radial functions. $Y^{\pm}_{j,j_z}(\hat{\Omega})$ are the spin-orbit coupled spherical harmonic functions with even and odd parities, respectively. For example, for the case of $j = j_z = \frac{1}{2}$, they are

$$Y^{+}_{\frac{1}{2},\frac{1}{2}}(r,\hat{\Omega}) = \begin{pmatrix} 1 \\ 0 \end{pmatrix}, \quad Y^{-}_{\frac{1}{2},\frac{1}{2}}(r,\hat{\Omega}) = \begin{pmatrix} \cos\theta \\ \sin\theta e^{i\phi} \end{pmatrix}, \tag{10}$$

the orbital partial-wave components of which are the s and p wave, respectively. The TR partner of Eq. (9) is $\psi_{j_z=-\frac{1}{2}} = \hat{T}\psi_{j=j_z=\frac{1}{2}} = i\sigma_2\psi^{*}_{j=j_z=\frac{1}{2}}$. The two terms in Eq. (9) are of opposite parity eigenvalues, mixed by the parity-breaking spin-orbit coupling $\vec{\sigma}\cdot\vec{p}$. The coefficient i of the $Y^{-}_{jj_z}$ term is due to the fact that the matrix element $\langle Y^{+}_{jj_z}|\vec{\sigma}\cdot\vec{p}|Y^{-}_{jj_z}\rangle$ is purely imaginary.

For the noninteracting case, the radial wave functions up to a Gaussian factor can be approximated by spherical Bessel functions as

$$f(r) \approx j_0(k_{\mathrm{SO}}r)e^{-r^2/2l_T^2}, \quad g(r) \approx j_1(k_{\mathrm{SO}}r)e^{-r^2/2l_T^2}, \tag{11}$$

which correspond to the s and p partial waves, respectively. Both of them oscillate along the radial direction and the pitch values are around k_{SO}. At $r = 0$, $f(r)$ reaches the maximum and $g(r)$ is zero. As r increases, roughly speaking, the zero points of $f(r)$ correspond to the extrema of $g(r)$ and vice versa. Repulsive interactions expand the spatial distributions of $f(r)$ and $g(r)$, but the above picture still holds qualitatively. In other words, there is a $\frac{\pi}{2}$-phase shift between the oscillations of $f(r)$ and $g(r)$.

B. The quaternion representation

Can we have unconventional BECs with nontrivial quaternionic condensate wave functions? Actually, the topological structure of condensate wave function Eq. (9) manifests clearly in the quaternion representation as shown below.

We define the following mapping from the complex two-component vector $\Psi = (\Psi_\uparrow, \Psi_\downarrow)^T$ to a quaternion variable through

$$\xi = \xi_0 + \xi_1 i + \xi_2 j + \xi_3 k, \tag{12}$$

where

$$\xi_0 = \mathrm{Re}\Psi_\uparrow, \xi_1 = \mathrm{Im}\Psi_\downarrow, \xi_2 = -\mathrm{Re}\Psi_\downarrow, \xi_3 = \mathrm{Im}\Psi_\uparrow. \tag{13}$$

i,j,k are the imaginary units satisfying $i^2 = j^2 = k^2 = -1$, and the anticommutation relation $ij = -ji = k$. The TR transformation on ξ is just $-j\xi$.

Equation (9) can be expressed in the quaternionic exponential form as

$$\xi_{j=j_z=\frac{1}{2}}(r,\hat{\Omega}) = |\xi(r)|e^{\vec{\omega}(\hat{\Omega})\gamma(r)} = |\xi|(\cos\gamma + \vec{\omega}\sin\gamma), \tag{14}$$

where

$$\begin{aligned} |\xi(r)| &= [f^2(r) + g^2(r)]^{\frac{1}{2}}, \\ \vec{\omega}(\hat{\Omega}) &= \sin\theta\cos\phi i + \sin\theta\sin\phi j + \cos\theta k, \\ \cos\gamma(r) &= f(r)/|\xi(r)|, \quad \sin\gamma(r) = g(r)/|\xi(r)|. \end{aligned} \tag{15}$$

$\omega(\hat{\Omega})$ is the imaginary unit along the direction of $\hat{\Omega}$ satisfying $\vec{\omega}^2(\hat{\Omega}) = -1$. According to the oscillating properties of $f(r)$ and $g(r)$, $\gamma(r)$ spirals as r increases. At the nth zero point of $g(r)$ denoted r_n, $\gamma(r_n) = n\pi$ where $n \geqslant 0$ and we define $r_0 = 0$, while at the nth zero point of $f(r)$ denoted r'_n, $\gamma(r'_n) = (n - \frac{1}{2})\pi$ where $n \geqslant 1$.

In three dimensions, the condensate wave functions can be topologically nontrivial because the homotopy group of the quaternionic phase is $\pi_3(S^3) = Z$ [25,26]. The corresponding winding number, i.e., the Pontryagin index, of the mapping $S^3 \to S^3$ is the 3D skyrmion number. The spatial distribution of the quaternionic phase $e^{\vec{\omega}(\hat{\Omega})\gamma(r)}$ defined in Eq. (14), which lies on S^3, exhibits a topologically nontrivial mapping from R^3 to S^3, i.e., a 3D multiple skyrmion configuration. This type of topological defect is nonsingular, which is different from the usual vortex in single-component BECs. In realistic trapping systems, the coordinate space is the open R^3. At large distance $r \gg l_T$, $|\xi(r)|$ decays exponentially, where the quaternionic phase and the mapping are not well defined. Nevertheless, in each concentric spherical shell with $r_n < r < r_{n+1}$, $\gamma(r)$ winds from $n\pi$ to $(n+1)\pi$, and $\omega(\hat{\Omega})$ covers all the directions, thus this shell contributes one to the winding number of $e^{\vec{\omega}(\hat{\Omega})\gamma(r)}$ on S^3. If the system size is truncated at the order of l_T, the skyrmion number can be approximated at the order of $l_T k_{\mathrm{SO}} = \alpha$.

There exists an interesting difference from the previously studied 2D case: Although the spin-density distribution exhibits the 2D skyrmion configuration due to $\pi_2(S^2)$ [6,17,18], the 2D condensation wave functions have no well-defined topology due to $\pi_2(S^3) = 0$.

C. The Hopf mapping and Hopf invariant

Exotic spin textures in spinor condensates have been extensively investigated [27–29]. In our case, the 3D spin-density distributions $\vec{S}(\vec{r})$ exhibit a novel configuration with nontrivial Hopf invariants due to the nontrivial homotopy group $\pi_3(S^2) = Z$ [25,26]. $\vec{S}(\vec{r})$ can be obtained from $\xi(r)$ through the first Hopf map defined as $\vec{S}(\vec{r}) = \frac{1}{2}\psi^{\dagger}_{\gamma}\vec{\sigma}_{\gamma\beta}\psi_{\delta}$, or, in the quaternionic representation,

$$\tfrac{1}{2}\bar{\xi}k\xi = S_x i + S_y j + S_z k, \tag{16}$$

where $\bar{\xi} = \xi_0 - \xi_1 i - \xi_2 j - \xi_3 k$ is the quaternionic conjugate of ξ. The Hopf invariant of the first Hopf map is just 1 [26]. The real-space concentric spherical shell $r_n < r < r_{n+1}$ maps to the quaternionic phase S^3, and the latter further maps to the S^2

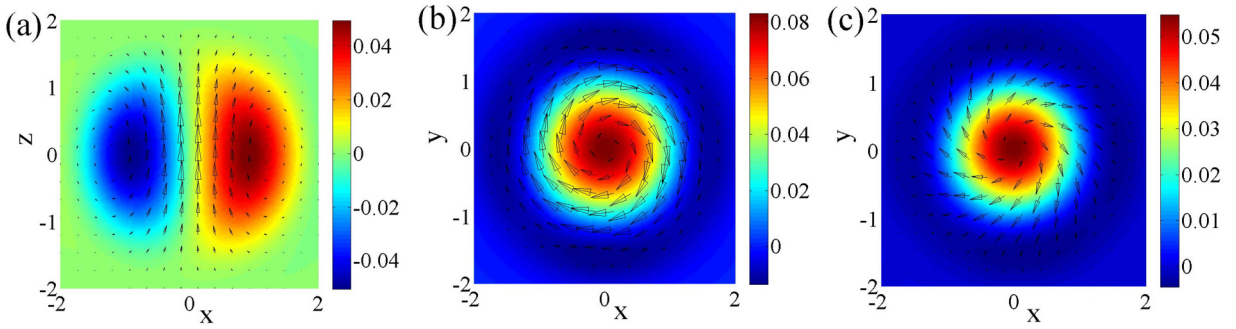

FIG. 1. The distribution of $\vec{S}(\vec{r})$ in (a) the xz plane and in the horizontal planes with (b) $z = 0$ and (c) $z/l_T = \frac{1}{2}$. The unit length is set as $l_T = 1$ in all the figures in this paper. The color scale shows the magnitude of out-plane component S_y in (a) and S_z in (b) and (c). The parameter values are $\alpha = 1.5$, $c = 1$, and $\beta = 30$, and the length unit in these and all the figures below is l_T.

Bloch sphere through the first Hopf map. The winding number of the first map is 1, and the Hopf invariant of the second map is also 1, thus the Hopf invariant of the shell $r_n < r < r_{n+1}$ to S^2 is 1. Rigorously speaking, the magnitude of $\vec{S}(\vec{r})$ decays exponentially at $r \gg l_T$, and thus the total Hopf invariant is not well defined in the open R^3 space. Again, if we truncate the system size at l_T, the Hopf invariant is approximately at the order of α.

Next we present numeric results for the spin textures associated with the condensation wave function Eq. (9) as plotted in Fig. 1. Explicitly, $\vec{S}(\vec{r})$ is expressed as

$$\begin{aligned} \begin{bmatrix} S_x(\vec{r}) \\ S_y(\vec{r}) \end{bmatrix} &= g(r)\sin\theta \begin{bmatrix} \cos\phi & -\sin\phi \\ \sin\phi & \cos\phi \end{bmatrix} \begin{bmatrix} g(r)\cos\theta \\ f(r) \end{bmatrix}, \\ S_z(\vec{r}) &= f^2(r) + g^2(r)\cos 2\theta. \end{aligned} \tag{17}$$

In the xz plane, the in-plane components S_x and S_z form a vortex in the half plane of $x > 0$ and S_y is prominent in the core. The contribution at large distance is neglected, where $\vec{S}(\vec{r})$ decays exponentially. Due to the axial symmetry of $\vec{S}(\vec{r})$ in Eq. (17), the 3D distribution is just a rotation of that in Fig. 1(a) around the z axis. In the xy plane, spin distribution exhibits a 2D skyrmion pattern, and the in-plane components are along the tangential direction. As the horizontal cross section shifts along the z axis, $\vec{S}(\vec{r})$ remains 2D skyrmionlike, but its in-plane components are twisted around the z axis. The spin configuration at $z = -z_0$ can be obtained by a combined operation of TR and rotation around the y axis 180°, thus its in-plane components are twisted in an opposite way compared to those at $z = z_0$. Combining the configurations on the vertical and horizontal cross sections, we complete the 3D distribution of $\vec{S}(\vec{r})$ with the nonzero Hopf invariant.

The nontrivial structure of the Hopf invariant of the above spin configuration can be revealed by plotting its Hopf fibration in terms of the linked noncrossing circles in real space, as shown in Fig. 2. For all the points on each circle, their normalized spin polarizations $\langle\vec{\sigma}\rangle/|\langle\vec{\sigma}\rangle|$ are the same, corresponding to a single point on the S^2 sphere. In addition, every two circles are linked with each other with the linking number 1, which is the standard Hopf bundle structure describing a many-to-one map from S^3 to S^2. Ultracold bosons with synthetic spin-orbit coupling provide a novel platform to study such beautiful mathematical ideas in realistic physics systems.

IV. THE INTERMEDIATE AND STRONG SPIN-ORBIT COUPLING REGIME

A. The intermediate spin-orbit coupling strength

Next we consider the case of the intermediate spin-orbit coupling strength, i.e., $1 < \alpha < 10$, at which the single-particle spectra evolve from the case of the harmonic potential to Landau-level-like as shown in Eq. (6). Interactions are sufficiently strong to mix a few lowest-energy states with different angular momenta j. As a result, rotational symmetry is broken and complex patterns appear.

In this case, the topology of condensate wave functions is still 3D skyrmionlike mapping from R^3 to S^3, and spin textures with the nontrivial Hopf invariant are obtained through the first Hopf map. Compared to the weak spin-orbit coupling case, the quaternionic phase skyrmions and spin textures are no longer concentric, but split to a multicentered pattern. The numeric results of $\vec{S}(\vec{r})$ are plotted in Fig. 3 for different horizontal cross sections. In the xy plane, $\vec{S}$ exhibits the 2D skyrmion pattern as shown in Fig. 3(b): The in-plane components form two vortices and one antivortex, while S_z's inside the vortex and antivortex cores are opposite in direction, thus they contribute to the skyrmion number with the same sign. The spin configuration at $z = z_0 > 0$ is shown in Fig. 3(a), which is twisted around

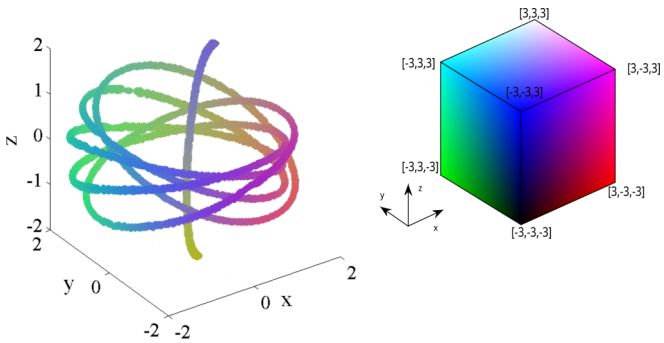

FIG. 2. The Hopf fibration of the spin texture configuration in Fig. 1. Every circle represents a spin orientation, and every two circles are linked with the linking number 1.

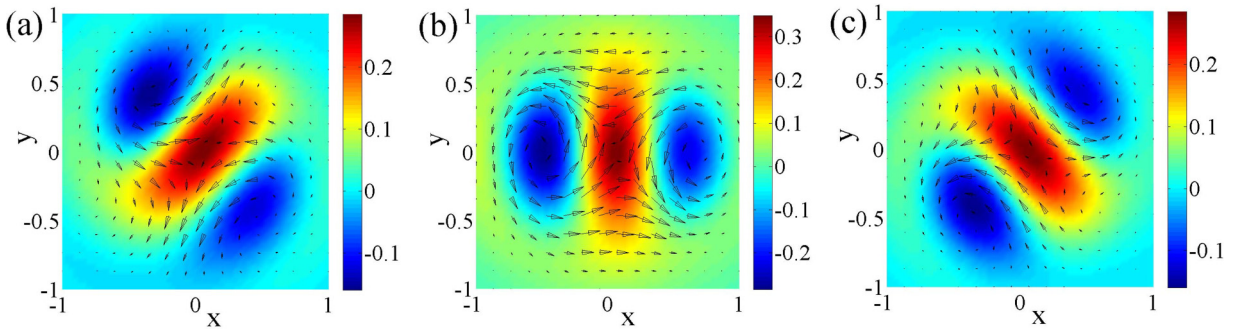

FIG. 3. The distribution of $\vec{S}(\vec{r})$ in horizontal cross-sections with (a) $z/l_T = -0.5$, (b) $z/l_T = 0$, and (c) $z/l_T = 0.5$, respectively. The color scale shows the value of S_z, and parameter values are $\alpha = 4$, $\beta = 2$, and $c = 1$.

the z axis clockwise. After performing the combined TR and rotation around the y axis 180°, we arrive at the configuration at $z = -z_0$ in Fig. 3(b).

B. The strong spin-orbit coupling regime

We next consider the case of strong spin-orbit coupling, i.e., $\alpha \gg 1$. The single-particle spectra already exhibit the Landau-level-type quantization in this regime as shown in Eq. (6). The single-particle eigenstates with $n_r = 0$ are nearly degenerate, i.e., they form the lowest Landau-level states. We assume that the interaction strength is enough to mix states inside the lowest Landau level but is still relatively weak not to induce inter-Landau-level mixing.

In this regime, the length scale of each skyrmion is shortened as enlarging the spin-orbit coupling strength. As we can imagine, more and more skyrmions appear and will form a 3D lattice structure, which is the SU(2) generalization of the 2D Abrikosov lattice of the usual U(1) superfluid. We have numerically solved the Gross-Pitaevskii equation (7) and found the lattice structure: Each lattice site is a single skyrmion of the condensate wave function $\xi(\vec{r})$, the spin configuration of which exhibits the texture configuration approximately with a unit Hopf invariant. The numeric results for the spin texture configuration are depicted in Figs. 4(a) and 4(b) for two different horizontal cross sections parallel to the xy plane. In each cross section, spin textures form a square lattice, and the lattice constant d is estimated approximately at the order of spin-orbit length scale as

$$d \simeq 2\pi l_{\mathrm{SO}} = 2\pi l_T/\alpha. \tag{18}$$

For two horizontal cross sections with a distance of $\Delta z \simeq d/2$, their square lattice configurations are displaced along the diagonal direction: The sites at one layer sit above the plaquette centers of the adjacent layer. As a result, the overall three-dimensional configuration of the topological defects is a body-centered cubic (bcc) lattice, and its size is finite confined by the trap.

V. THE EFFECT OF STRONG INTERACTIONS

In this section, we present the condensate configurations in the case that both spin-orbit coupling and interactions are strong, such that different Landau levels are mixed by interactions.

In this case, the effect of the harmonic trapping potential becomes weak compared with interaction energies, thus we can approximate the condensate wave functions as superpositions of plane-wave states. The plane-wave components are located on the spin-orbit sphere and the condensate wave functions are no longer topological. At $c = 1$, the interaction is spin independent, and bosons select a superposition of a pair of states $\pm\vec{k}$ on the spin-orbit sphere, say, $\pm k_{\mathrm{SO}}\hat{z}$. The condensate

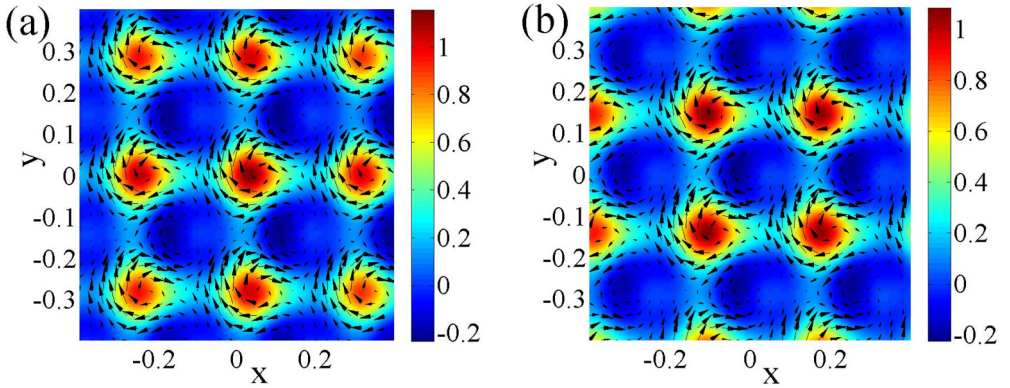

FIG. 4. The distribution of $\vec{S}(\vec{r})$ in horizontal cross-sections with (a) $z/l_T = 0$ and (b) $z/l_T = 0.2$. The color scale shows the value of S_z and parameter values are $\alpha = 22$, $\beta = 1$, and $c = 1$. The overall lattice exhibits the bcc structure.

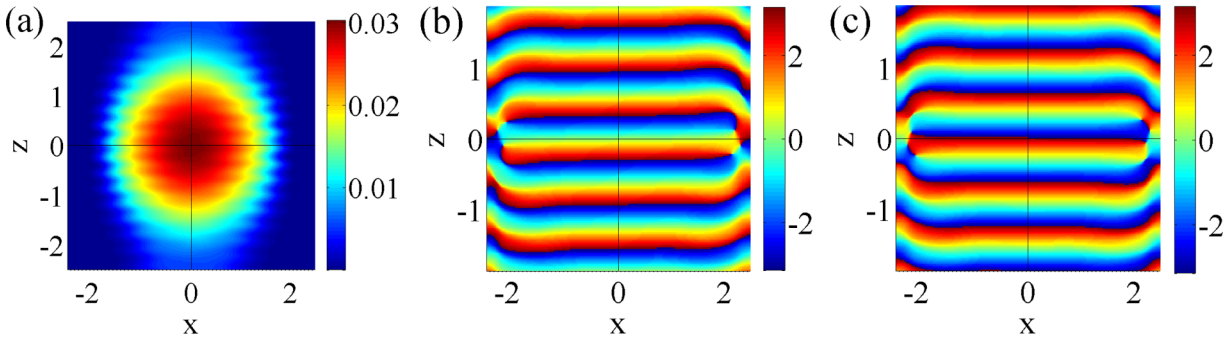

FIG. 5. (a) The density profile for the ↑ component, and that for the ↓ component is the same. Phase profiles are also shown for (b) ↑ and (c) ↓ components. Parameter values are $a = 10$, $\beta = 50$, and $c = 0.5$.

wave function is written as

$$\psi(\vec{r}) = \sqrt{\frac{N_a}{N_0}} e^{ik_{SO}z} |\uparrow\rangle + \sqrt{\frac{N_b}{N_0}} e^{-ik_{SO}z} |\downarrow\rangle, \tag{19}$$

with $N_a + N_b = N_0$. The density of Eq. (19) in real space is uniform to minimize the interaction energy at the Hartree-Fock level. However, all the different partitions of $N_{a,b}$ yield the same Hartree-Fock energy. The quantum zero-point energy from the Bogoliubov modes removes this accidental degeneracy through the "order-from-disorder" mechanism, which selects the equal partition $N_a = N_b$. The calculation is in parallel to that of the 2D Rashba case performed in Ref. [6], and thus will not be presented here. In this case, the condensate is a spin helix propagating along the z axis and spin spirals in the xy plane.

At $c \neq 1$, the spin-dependent part of the interaction can be written as

$$H_{sp} = \frac{1-c}{2} g \int d^3r (\psi_\uparrow^\dagger \psi_\uparrow - \psi_\downarrow^\dagger \psi_\downarrow)^2. \tag{20}$$

At $c > 1$, the interaction energy at Hartree-Fock level is minimized for the condensate wave function of a plane-wave state $e^{ik_{SO}z}|\uparrow\rangle$ or its TR partner.

For $c < 1$, $\langle H_{sp} \rangle$ is minimized if $\langle S_z \rangle = 0$ in space. At the Hartree-Fock level, the condensate can either be a plane-wave state with momentum lying in the equator of the spin-orbit sphere and spin polarizing in the xy plane or the spin spiral state described by Eq. (19) with $N_a = N_b$. An order-from-disorder analysis on the Bogoliubov zero-point energies indicates that the spin spiral state is selected. We also present the numerical results for Eq. (4) in the main text with a harmonic trap in Fig. 5 for the case of $c < 1$. The condensate momenta of two spin components have opposite signs, thus the trap inhomogeneity already prefers the spin spiral state Eq. (19) at the Hartree-Fock level.

VI. CONCLUSION

In summary, we have investigated the two-component unconventional BECs driven by the 3D spin-orbit coupling. In the quaternionic representation, the quaternionic phase distributions exhibit nontrivial 3D skyrmion configurations from R^3 to S^3. The spin orientation distributions exhibit texture configurations characterized by nonzero Hopf invariants from R^3 to S^2. These two topological structures are connected through the first Hopf map from S^3 to S^2. At large spin-orbit coupling strength, the crystalline order of spin textures, or wave function skyrmions, are formed, which can be viewed as a generalization of the Abrikosov lattice in three dimensions.

Note added. We have also seen quick progress on the topic studied in this paper in recent years. The 3D spin-orbit coupled BECs are studied in Refs. [30,31] focusing on the single skyrmion configuration under the Gross-Pitaevskii framework. The spectrum of a single particle with the 3D spin-orbit coupling combined with a harmonic trap is solved in Ref. [32]. The spin-orbit coupled BEC-to-Mott insulator transition in the optical lattice is studied in Ref. [33]. The skyrmion crystal states of spin-$\frac{1}{2}$ bosons without spin-orbit coupling are solved in Refs. [34,35]. Furthermore, the magnetic and nematic phases are numerically solved for the spin-1 bosons with the 3D spin-orbit coupling in Ref. [36].

ACKNOWLEDGMENTS

Y.L. thanks the Princeton Center for Theoretical Science at Princeton University for support. X.F.Z. acknowledges the support of NFRP (Grants No. 2011CB921204 and No. 2011CBA00200), the Strategic Priority Research Program of the Chinese Academy of Sciences (Grant No. XDB01030000), NSFC (Grants No. 11004186 and No. 11474266), and the Major Research plan of the National Natural Science Foundation of China (Grant No. 91536219). C.W. is supported by NSF Grant No. DMR-1410375 and AFOSR Grant No. FA9550-14-1-0168. C.W. acknowledges support from the President's Research Catalyst (Award No. CA-15-327861) from the University of California Office of the President, National Natural Science Foundation of China (Grant No. 11328403), and support by the CAS/SAFEA International Partnership Program for Creative Research Teams.

[1] R. P. Feynman, *Statistical Mechanics, A Set of Lectures* (Addison-Wesley, Berlin, 1972).

[2] R. B. Bapat and T. Raghavan, *Non-Negative Matrices and Applications* (Cambridge University, Cambridge, England, 1997).

[3] A. J. Leggett, Rev. Mod. Phys. **73**, 307 (2001).

[4] C. Wu, Mod. Phys. Lett. **23**, 1 (2009).

[5] X. F. Zhou, Y. Li, Z. Cai, and C. Wu, J. Phys. B **46**, 134001 (2013).

[6] C. Wu and I. Mondragon-Shem, arXiv:0809.3532v1; C. Wu, I. Mondragon-Shem, and X. F. Zhou, Chin. Phys. Lett. **28**, 097102 (2011).
[7] A. A. High, J. R. Leonard, A. T. Hammack, M. M. Fogler, L. V. Butov, A. V. Kavokin, K. L Campman, and A. C. Gossard, Nature (London) **483**, 584 (2012).
[8] A. A. High, A. T. Hammack, J. R. Leonard, S. Yang, L. V. Butov, T. Ostatnicky, M. Vladimirova, A. V. Kavokin, T. C. H. Liew, K. L. Campman, and A. C. Gossard, Phys. Rev. Lett. **110**, 246403 (2013).
[9] Y.-J. Lin, R. L. Compton, K. Jimenez-Garcia, J. V. Porto, and I. B. Spielman, Nature (London) **462**, 628 (2009).
[10] Y. J. Lin, K. Jimenez-Garcia, and I. B. Spielman, Nature (London) **471**, 83 (2011).
[11] T. D. Stanescu, B. Anderson, and V. Galitski, Phys. Rev. A **78**, 023616 (2008).
[12] T.-L. Ho and S. Zhang, Phys. Rev. Lett. **107**, 150403 (2011).
[13] C. Wang, C. Gao, C. M. Jian, and H. Zhai, Phys. Rev. Lett. **105**, 160403 (2010).
[14] S.-K. Yip, Phys. Rev. A **83**, 043616 (2011).
[15] Y. Zhang, L. Mao, and C. Zhang, Phys. Rev. Lett. **108**, 035302 (2012).
[16] X. F. Zhou, J. Zhou, and C. Wu, Phys. Rev. A **84**, 063624 (2011).
[17] Hui Hu, B. Ramachandhran, Han Pu, and Xia-Ji Liu, Phys. Rev. Lett. **108**, 010402 (2012).
[18] S. Sinha, R. Nath, and L. Santos, Phys. Rev. Lett. **107**, 270401 (2011).
[19] Y. Li, X. F. Zhou, and C. Wu, Phys. Rev. B **85**, 125122 (2012).
[20] B. M. Anderson, G. Juzeliunas, V. M. Galitski, and I. B. Spielman, Phys. Rev. Lett. **108**, 235301 (2012).
[21] A. V. Balatsky, arXiv:cond-mat/9205006.
[22] S. L. Adler, *Quaternionic Quantum Mechanics and Quantum Fields* (Oxford University, Oxford, 1995).
[23] D. Finkelstein, J. M. Jauch, S. Schiminovich, and D. Speiser, J. Math. Phys. (NY) **3**, 207 (1962).
[24] S. K. Ghosh, J. P. Vyasanakere, and V. B. Shenoy, Phys. Rev. A **84**, 053629 (2011).
[25] F. Wilczek and A. Zee, Phys. Rev. Lett. **51**, 2250 (1983).
[26] M. Nakahara, *Geometry, Topology, and Physics*, (Taylor and Francis, London, 2003).
[27] F. Zhou, Int. J. Mod. Phys. B **17**, 2643 (2003); E. Demler and F. Zhou, Phys. Rev. Lett. **88**, 163001 (2002); G. W. Semenoff and F. Zhou, *ibid.* **98**, 100401 (2007).
[28] J. Zhang and T. L. Ho, J. Low Temp. Phys. **161**, 325 (2010).
[29] D. M. Stamper-Kurn and M. Ueda, Rev. Mod. Phys. **85**, 1191 (2013).
[30] T. Kawakami, T. Mizushima, M. Nitta, and K. Machida, Phys. Rev. Lett. **109**, 015301 (2012).
[31] Guanjun Chen, Tiantian Li, and Yunbo Zhang, Phys. Rev. A **91**, 053624 (2015).
[32] Brandon M. Anderson and Charles W. Clark, J. Phys. B **46**, 134003 (2013).
[33] Dan-Wei Zhang, Ji-Pei Chen, Chuan-Jia Shan, Z. D. Wang, and Shi-Liang Zhu, Phys. Rev. A **88**, 013612 (2013).
[34] Cong Zhang, Wen-An Guo, Shi-Ping Feng, and Shi-Jie Yang, Chinese Physics B **22**, 110308 (2013).
[35] Yong-Kai Liu and Shi-Jie Yang, Chinese Physics B **23**, 110308 (2014).
[36] Guanjun Chen, Li Chen, and Yunbo Zhang, arXiv:1512.06394.